A CRITICAL COMPARISON OF LINEAR AND NONLINEAR UNMIXING FOR INTIMATE MIXTURES

Bikram Koirala[1] Samiran Das[2], Behnood Rasti[2], Pedram Ghamisi[2], Richard Gloaguen[2], Paul Scheunders[1]

[1] Imec-Visionlab, University of Antwerp (CDE) Universiteitsplein 1, B-2610 Antwerp
[2] Helmholtz-Zentrum Dresden-Rossendorf (HZDR), Helmholtz Institute Freiberg for Resource Technology.

ABSTRACT

In this study, we conducted a comparative analysis of various linear and nonlinear unmixing methods to estimate the composition of intricate clay powder mixtures based on their spectral reflectance. Our experiments were conducted using industrial clay powder mixtures generated in a laboratory. Specifically, we created 325 uniform mixtures by combining five types of clay powders: Kaolin, Roof clay, Red clay, mixed clay, and Calcium hydroxide. Among these 325 samples, 60 were binary mixtures, 150 were ternary mixtures, 100 were quaternary mixtures, and 15 were quinary mixtures. We acquired spectral data by scanning these samples using two handheld spectrometers (ASD Spectroradiometer and PSR-3500 spectral evolution) and two hyperspectral cameras (Specim AsiaFenix and Specim sCMOS). We applied several state-of-the-art unmixing methods to the generated datasets. The experimental findings indicate that specialized nonlinear unmixing methods are necessary for accurate estimation of the fractional abundances in these complex mixtures.

Index Terms— Hyperspectral image, linear and nonlinear unmixing, intimate mixtures

1. INTRODUCTION

Hyperspectral unmixing techniques estimate the fractional abundances of various materials within a pixel's field of view by minimizing the discrepancy between the measured spectral reflectance and the spectrum generated through a specific mixing model. The linear mixing model (LMM) is the most widely used mixing model in the remote sensing community. It assumes that each incident ray of light interacts with a single pure material in the instantaneous field of view of the pixel before being detected by the sensor. To account for the physical constraints of non-negativity and sum-to-one for fractional abundances, the Fully Constrained Least Squares Unmixing procedure (FCLSU) was introduced [1]. However, the linear mixing model proves inadequate when incident light undergoes multiple reflections before reaching the sensor [2, 3].

Nonlinear mixing models have been developed to explain the complex interaction of light with the target's surface [4, 5]. Bilinear mixing models (e.g., PPNM [6, 7] and GBM ([8, 9]) assume that an incident ray of light interacts with two pure materials before reaching the sensor. To explain higher-order interactions, multilinear mixing models (e.g., [10]) and intimate mixture models (e.g., [11, 12]) have been developed.

Among existing mixing models, physics-based mixing models such as the Hapke model [11] are found to be suitable for analyzing the spectral reflectance of intimate mixtures, only when the material grains/particles have a size, larger than the wavelength of the light, their shape is spherical, and they behave as isotropic scatterers. In reality, most of the particles are non-spherical, and grain size varies between a few micrometers to a few hundred micrometers, leading to a low performance of the Hapke model on natural mixtures.

To assess the efficacy of spectral unmixing models in estimating the composition of intimate mixtures, we created a comprehensive dataset consisting of intimate mixtures involving up to five pure clay powders: Kaolin, Roof clay, Red clay, mixed clay, and Calcium hydroxide. This dataset, in total, consists of 330 samples. Among these, five samples are pure clay powders, 60 mixtures are binary, 150 mixtures are ternary, 100 mixtures are quaternary, and 15 mixtures are quinary. The spectral reflectance of these samples is acquired by four sensors utilizing various acquisition configurations, covering the visible near-infrared and shortwave infrared wavelength regions (350 nm - 2500 nm). We conducted an extensive series of experiments with these datasets, especially focusing on estimating endmembers and fractional abundances of these mixtures. This estimation was performed using three linear and five nonlinear unmixing methods.

2. HYPERSPECTRAL DATA DESCRIPTION

Recently, we prepared a comprehensive laboratory ground truth dataset of intimately mixed mineral powders [13]. This dataset was prepared by homogeneously mixing five pure clay powders: Kaolin, Roof clay, Red clay, mixed clay, and Calcium hydroxide. All possible clay combinations of these powders were considered, i.e., 5 pure clay powders, 10 binary combinations (Kaolin-Roof clay, Kaolin-Red clay, Kaolin-Mixed clay, Kaolin-Calcium hydroxide, Roof clay-Red clay, Roof clay-Mixed clay, Roof clay-Calcium hydroxide,

Red clay-Mixed clay, Red clay-Calcium hydroxide, Mixed clay-Calcium hydroxide), 10 ternary combinations (Kaolin-Roof clay-Red clay, Kaolin-Roof clay-Mixed clay, Kaolin-Roof clay-Calcium hydroxide, Kaolin-Red clay-Mixed clay, Kaolin-Red clay-Calcium hydroxide, Kaolin-Mixed clay-Calcium hydroxide, Roof clay-Red clay-Mixed clay, Roof clay-Red clay-Calcium hydroxide, Roof clay-Mixed clay-Calcium hydroxide, Red clay-Mixed clay-Calcium hydroxide), 5 quaternary combinations (Kaolin-Roof clay-Red clay-Mixed clay, Kaolin-Roof clay-Red clay-Calcium hydroxide, Kaolin-Roof clay-Mixed clay-Calcium hydroxide, Kaolin-Red clay-Mixed clay-Calcium hydroxide, Roof clay-Red clay-Mixed clay-Calcium hydroxide), and one quinary combination (Kaolin-Roof clay-Red clay-Mixed clay-Calcium hydroxide).

Within each clay combination, samples with different mixture fractions are generated in such a way that the ground truth fractional abundances uniformly cover the simplex. The chosen step size between mass ratios is 14.286%. Following this approach, six unique mixtures are generated for each binary clay combination, 15 for the ternary clay combination, 20 for the quaternary clay combination, and 15 for the quinary clay combination, making a total of 325 mixtures. As an illustration, Fig. 1 showcases the ground truth fractional abundances for a ternary clay combination. As can be observed, the three pure clay powders are located at the corners of the simplex. All binary mixtures are positioned at the lines that connect two pure clay powders, while ternary mixtures are located inside the simplex.

To create the mixtures, we weighed and combined the pure components. Each sample had a fixed total weight of 10 g (with a precision of 0.001 g on the scale). Each 10 g sample was placed inside a glass bottle and rotated continuously for five minutes to ensure a thorough and homogeneous mixture.

Using the particle densities of the pure clays, we converted the mass fractions to volume fractions by:

$$a_j = \frac{\frac{M_j}{\rho_j}}{\sum_{j=1}^{p} \frac{M_j}{\rho_j}}, \quad (1)$$

where p denotes the number of pure clays involved in the mixture, M_j is the mass fraction of the j-th pure clay, and ρ_j its density. The samples were placed inside a clear plastic jar with an interior diameter of 3.048 cm and a height of 1.524 cm. Approximately 3 g of the mixtures was required to fill the sample holder. The samples were then compacted and smoothed using a stamp compactor.

In the next step, all samples were scanned by 4 different sensors. Two hand-held spectroradiometers: ASD and PSR-3500 spectral evolution generate a single spectrum of each sample. Two hyperspectral cameras: a Specim AisaFenix and a Specim sCMOS generated a hyperspectral data cube. Table 1 summarizes the properties of these sensors. The radiance

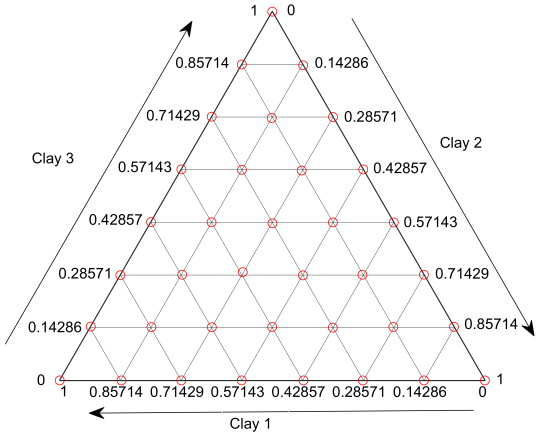

Fig. 1. The ternary diagram of clay mixtures.

data captured by the Specim AsiaFenix and Specim sCMOS cameras were converted to reflectance using an internal workflow based on Hylite [14]. The spectra acquired by the hyperspectral cameras were averaged over the entire sample surface for further analysis.

The datasets can be downloaded from the following link: `https://github.com/VisionlabHyperspectral/Multisensor_datasets`.

3. EXPERIMENTS

3.1. Experimental Setup

Because existing state-of-the-art unmixing methods require a hyperspectral dataset as input, for each sensor, we generated a matrix by assembling the spectral reflectances of all 330 samples (325 mixtures and 5 pure pixels). This matrix was further reshaped to produce hyperspectral data of size $22\times15\times$#bands. Note that there is no spatial relationship between neighboring pixels in this image. For a fair comparison, all methods in our experiment are blind unmixing approaches, i.e., they extract or estimate endmembers and estimate the fractional abundances of the input hyperspectral data. The following unmixing methods were considered in the experiments:

- Geometrical unmixing: VCA [15] is applied for endmember extraction and FCLSU [16] for abundance estimation. In this work, we will refer to this procedure as FCLSU.
- A Deep Neural Network for Blind Unmixing: MiSiC-Net [3].
- Geometrical and blind linear unmixing: NMF-QMV [2].
- Bilinear unmixing: PPNM [6]. Endmembers are obtained using VCA. Hereafter, abundances are estimated

Table 1. Properties of sensors employed in this study

Sensor	Spectral range	Bands/Channels	Spatial resolution	Spectral resolution
ASD Spectroradiometer	350 nm to 2500 nm	2151	-	3-6 nm
PSR-3500 spectral evolution	350 nm to 2500 nm	1024	-	2.8-8 nm
Specim AisaFenix	400 nm to 2500 nm	450	1024 pixels	3.5-10 nm
Specim sCMOS	400 nm to 1000 nm	238	2148 pixels	6 nm

by bilinear unmixing.

- Blind nonlinear unmixing: Deep Autoencoder based on PPNM (MAC-U) [7]. VCA was applied for initializing the endmembers.
- Bilinear unmixing: Nonnegative Tensor Factorization (LR-NTF) [9]. Endmembers are obtained using VCA. Hereafter, abundances are estimated by Nonnegative Tensor Factorization.
- Multilinear unmixing: MLM [10]. Endmembers are obtained using VCA. Hereafter, abundances are estimated by multilinear unmixing.
- Intimate unmixing: Hapke[11]. Endmembers are obtained using VCA. Hereafter, abundances are estimated by applying the Hapke model.

For all methods, the default parameters provided by the authors were used. All quantitative comparisons are provided by the abundance root mean squared error (RMSE), i.e. the error between the estimated fractional abundances ($\hat{\mathbf{A}}$) and the ground truth fractional abundances ($\mathbf{A}$):

$$\text{Abundance RMSE} = \sqrt{\frac{1}{pm}\sum_{k=1}^{p}\sum_{i=1}^{m}\left(\hat{\mathbf{A}}_{ki} - \mathbf{A}_{ki}\right)^2} \times 100 \tag{2}$$

and the spectral angle distance (SAD) in degree between the estimated and ground-truth endmembers:

$$\text{SAD}(\mathbf{E}, \hat{\mathbf{E}}) = \frac{1}{p}\sum_{i=1}^{p}\arccos\left(\frac{\left\langle \mathbf{e}_{(i)}, \hat{\mathbf{e}}_{(i)}\right\rangle}{\left\|\mathbf{e}_{(i)}\right\|_2 \left\|\hat{\mathbf{e}}_{(i)}\right\|_2}\right) \times 180/\pi, \tag{3}$$

where p and m denote the number of endmembers and the number of mixed spectra, respectively, $\langle . \rangle$ denotes the inner product and $\mathbf{e}_{(i)}$ indicates the ith column of the ground truth endmembers matrix $\mathbf{E}$.

3.2. Unmixing Experiments

We applied the state-of-the-art unmixing methods to the individual datasets acquired by the four sensors (Specim AisaFenix, ASD Spectroradiometer, PSR-3500 spectral evolution, and Specim sCMOS). Table 2 and Table 3 show the RMSE and the SAD by all unmixing methods. In general, the abundance estimation performance is low (i.e., RMSE is high). Among the competing methods, MLM performed the best on the Specim AisaFenix and ASD Spectroradiometer data, while NMF_QMV outperformed others on the PSR-3500 spectral evolution and Specim sCMOS data. Even though LR_NTF is based on PPNM, its performance was lower than PPNM itself for most of the datasets. The Hapke model, which was developed to analyze intimate mixtures, did not perform better than the linear (FCLSU), bilinear (PPNM), and multilinear mixing models (MLM). This demonstrates the high complexity of these mixtures.

Table 2. Abundance RMSE (in %). The best performances are shown in bold.

	AISA	ASD	PSR	sCMOS
MLM	**18.97**	**12.61**	17.93	32.34
PPNM	22.80	33.13	20.26	22.60
FCLSU	19.26	21.31	18.05	29.26
Hapke	21.06	33.51	18.68	29.13
MAC-U	20.46	12.71	19.03	20.46
MiSiCNet	28.85	27.34	27.13	29.20
NMF_QMV	22.08	21.42	**14.63**	**17.42**
LR_NTF	57.02	30.13	39.37	34.02

Table 3. SAD (in degree). The best performances are shown in bold.

	AISA	ASD	PSR	sCMOS
VCA	2.12	0.92	**1.75**	1.25
MAC-U	**2.08**	**0.55**	1.81	**0.99**
MiSiCNet	4.06	4.23	4.80	2.48
NMF_QMV	7.11	7.99	4.26	4.74

The acquired SAD values are relatively low, indicating a favorable performance in endmember extraction. Fig. 2 displays both the ground truth endmembers (depicted in red) and the endmembers extracted/estimated by the competing methods. Because the datasets contain pure spectra, VCA was able to extract most of the endmembers properly (see overlapping red and black lines). Although both MiSiCNet and NMF_QMV are powerful blind linear unmixing methods, they were not able to accurately estimate the endmembers. This can be partially attributed to the nonlinearity of the components. It is interesting to observe that the SAD value

of MAC-U is the lowest (as shown in Table 3) for the ASD Spectroradiometer, However, the absolute reflectance values exhibit significant deviation from the ground truth (as indicated by the blue curves). It is important to highlight that SAD is scale-invariant and, as such, should not be exclusively relied upon for endmember evaluation.

4. CONCLUSIONS

We conducted a comparative analysis involving linear and nonlinear mixing methods using an extensive dataset of spectral reflectance from intimate clay powder mixtures. The experimental results indicate that accurate extraction of endmembers can be achieved when pure pixels are present in the dataset. On the other hand, the estimation of fractional abundances within the context of intimate mixtures poses a more intricate challenge.

5. REFERENCES

[1] J. W. Boardman, "Geometric mixture analysis of imaging spectrometry data," in *IEEE International Geoscience and Remote Sensing Symposium*, 1994, pp. 2369–2371.

[2] L. Zhuang, C. Lin, M. A. T. Figueiredo, and J. M. Bioucas-Dias, "Regularization parameter selection in minimum volume hyperspectral unmixing," *IEEE Transactions on Geoscience and Remote Sensing*, vol. 57, no. 12, pp. 9858–9877, 2019.

[3] B. Rasti, B. Koirala, P. Scheunders, and J. Chanussot, "Misicnet: Minimum simplex convolutional network for deep hyperspectral unmixing," *IEEE Transactions on Geoscience and Remote Sensing*, pp. 1–1, 2022.

[4] R. Heylen, M. Parente, and P. Gader, "A review of nonlinear hyperspectral unmixing methods," *IEEE Journal of Selected Topics in Applied Earth Observations and Remote Sensing*, vol. 7, no. 6, pp. 1844–1868, 2014.

[5] N. Dobigeon, J.Y. Tourneret, C. Richard, Jose Carlos M. Bermudez, Stephen McLaughlin, and Alfred O. Hero, "Nonlinear unmixing of hyperspectral images," *IEEE Signal Processing Magazine*, vol. 31, no. 1, pp. 82–94, JAN 2014.

[6] Y. Altmann, A. Halimi, N. Dobigeon, and J. Tourneret, "Supervised nonlinear spectral unmixing using a postnonlinear mixing model for hyperspectral imagery," *IEEE Transactions on Image Processing*, vol. 21, no. 6, pp. 3017–3025, 2012.

[7] H. Li, R. A. Borsoi, T. Imbiriba, P. Closas, J. C. M. Bermudez, and D. Erdoğmuş, "Model-based deep autoencoder networks for nonlinear hyperspectral unmixing," *IEEE Geoscience and Remote Sensing Letters*, vol. 19, pp. 1–5, 2022.

[8] A. Halimi, Y. Altmann, N. Dobigeon, and J. Tourneret, "Nonlinear unmixing of hyperspectral images using a generalized bilinear model," *IEEE Transactions on Geoscience and Remote Sensing*, vol. 49, no. 11, pp. 4153–4162, 2011.

[9] L. Gao, Z. Wang, L. Zhuang, H. Yu, B. Zhang, and J. Chanussot, "Using low-rank representation of abundance maps and nonnegative tensor factorization for hyperspectral nonlinear unmixing," *IEEE Transactions on Geoscience and Remote Sensing*, vol. 60, pp. 1–17, 2022.

[10] R. Heylen and P. Scheunders, "A multilinear mixing model for nonlinear spectral unmixing," *IEEE Transactions on Geoscience and Remote Sensing*, vol. 54, no. 1, pp. 240–251, Jan 2016.

[11] B. Hapke, "Bidirectional reflectance spectroscopy: 1. theory," *Journal of Geophysical research*, vol. 86, pp. 3039–3054, 1981.

[12] B. Rasti, B. Koirala, and P. Scheunders, "Hapkecnn: Blind nonlinear unmixing for intimate mixtures using hapke model and convolutional neural network," *IEEE Transactions on Geoscience and Remote Sensing*, vol. 60, pp. 1–15, 2022.

[13] B. Koirala, B. Rasti, Z. Bnoulkacem, A. d. L. R., Y. M., E. Herrmann, A. Gestels, T. D. Kerf, S. Lorenz, M. Fuchs, K. Janssens, G. Steenackers, R. Gloaguen, and P. Scheunders, "A multisensor hyperspectral benchmark dataset for unmixing of intimate mixtures," *arXiv*, 2023.

[14] S. T. Thiele, S. Lorenz, M. Kirsch, I. C. C. Acosta, L. Tusa, E. Herrmann, R. Möckel, and R. Gloaguen, "Multi-scale, multi-sensor data integration for automated 3-d geological mapping," *Ore Geology Reviews*, vol. 136, pp. 104252, 2021.

[15] J. Nascimento and J. Bioucas-Dias, "Vertex component analysis: A˜fast algorithm to extract endmembers spectra from hyperspectral data," in *Pattern Recognition and Image Analysis*, Francisco José Perales, Aurélio J. C. Campilho, Nicolás Pérez de la Blanca, and Alberto Sanfeliu, Eds., Berlin, Heidelberg, 2003, pp. 626–635, Springer Berlin Heidelberg.

[16] D. C. Heinz and Chein-I-Chang, "Fully constrained least squares linear spectral mixture analysis method for material quantification in hyperspectral imagery," *IEEE Transactions on Geoscience and Remote Sensing*, vol. 39, no. 3, pp. 529–545, 2001.

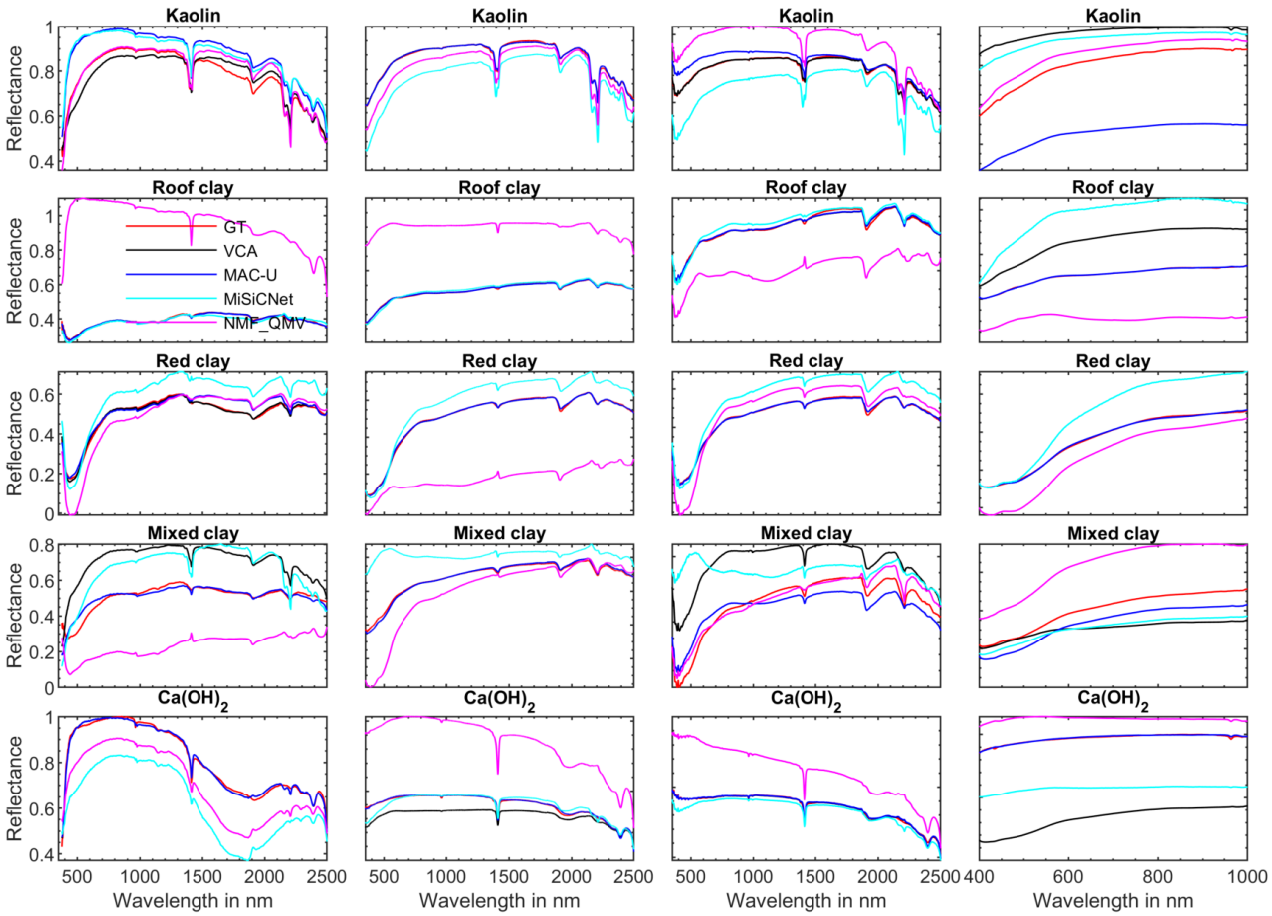

Fig. 2. Endmembers extracted/estimated by the competing techniques from the dataset acquired by (a) Specim AisaFenix; (b)ASD Spectroradiometer; (c) PSR-3500 spectral evolution; (d) Specim sCMOS. The figure shows ground truth endmembers (in red) alongside the endmembers estimated by VCA (black), MAC-U (blue), MiSiCNet (cyan) and NMF_QMV (magenta), respectively.